THE BEAM LOSS DETECTION SYSTEM OF THE LHC RING

E. Gschwendtner, B. Dehning, G. Ferioli, W. Friesenbichler, V. Kain

CERN, Geneva, Switzerland

Abstract

At the Large Hadron Collider (LHC) a beam loss system will be installed in the arc, dispersion suppressor and the straight regions for a continuous surveillance of particle losses. These beam particles deposit their energy partially in the super-conducting coils leading to temperature increase, possible magnet quenches and damages. The primary and secondary halo of the beam is absorbed by the collimation system. The tertiary halo will be lost at aperture limits in the ring. Its loss distribution along the magnets has been studied.

At the positions, where most of the beam losses are expected, simulations of the particle fluences outside the cryostat and induced by lost protons at the aperture have been performed with the Monte Carlo Code Geant 3.21. This allows determining the most suitable positions of the detectors, the needed number of monitors and the impact on the dynamic range of the detectors. The design of the beam loss monitor system is presented that meet the required sensitivity, dynamic range and time resolution.

1 INTRODUCTION

At the nominal energy of 7TeV each beam in the LHC stores energy of up to 0.35GJ. The loss of only a fraction (10^{-8}) of the beam can have a severe impact on the smooth machine operation. Therefore the beam loss detection system must fulfil several requirements:

- *Protection*: The magnets and other equipments must be protected from damage due to beam losses. E.g. repairing a magnet introduces a machine downtime of several weeks.
- *Prevention*: Beam losses that could lead to a quench of a super-conducting magnet must be detected, in order to dump the beam shortly before.
- *Beam diagnostic tool*: Beam loss monitors can be used to optimise the accelerator tuning.

For protection and prevention the beam loss monitors trigger the beam dump via the beam interlock system, whenever they detect beam losses above a certain limit. The quench levels of the super-conducting magnets define this limit.

1.1 Quench levels

The coils of the magnets can quench if a local deposition of energy due to beam particle losses increases the coil temperature to a value where the conductor changes from super-conducting to normal conducting. The different quench processes are described in detail in [1] and [2]. In addition to the energy dependence of the quench levels, a strong dependence on the duration of the loss is observed.

At 450GeV the quench limit is $1.1 \cdot 10^9$ protons/m for a loss duration of 1 turn (89µs) and $7 \cdot 10^8$ protons/m/s. At 7TeV the magnets quench after $9 \cdot 10^5$ lost protons/m per turn and after $7.6 \cdot 10^6$ p/m/s.

1.2 Beam loss sources

Under steady beam conditions, the primary and secondary collimators in the cleaning insertions define the aperture limitations in the ring. Hence beam losses induced by injection errors, asynchronous dump kickers [3], fast amplitude growth due to tripping of some magnets [4], etc. will first be located in these regions.

However, the tertiary beam halo, which is emitted by the secondary collimators, will be lost at local aperture limitations in the ring. Local losses can be caused by e.g. a local orbit excursion that exceeds 4mm or a β-beat of 20%. So this kind of beam loss is mainly relevant at locations with high β-functions or where mechanical limitations of the aperture can be assumed.

In the following chapters we concentrate on the beam losses in the ring due to the tertiary halo.

2 LONGITUDINAL BEAM LOSS DISTRIBUTION

A tertiary halo has been generated with a vertically primary halo hitting the collimators. The vertical coordinate (Y) of the particles is uncorrelated with the gaussian distributed horizontal coordinate (X). In order to study beam losses along critical locations, we look nearby defocusing quadrupoles, where the vertical β-function is maximal. The halo data are prepared for tracking through the interesting elements via transfer-matrices that depend on the lattice functions of the last collimator and the first element of the considered structure. The structure contains a short section of the LHC, consisting of the elements dipole(14.3m)-drift(1.8m)-quadrupole(0.3m)-drift(0.3m)-quadrupole(3.1m)-drift(2.4m)-dipole(14.3m). From the first element on, the particles in the halo are tracked through each element with a slice-length of 0.1m. Whenever a particle hits the aperture, it is lost.

The left plot in Fig.1 shows the particle loss distribution along the elements. The halo size is 12σ, with 1σ=1.2mm for 450GeV in the quadrupole (for 7TeV 1σ=0.3mm with β_y=180m, ε_{7TeV}=0.5nmrad, ε_{450GeV}=8nmrad). We have assumed a vertical orbit excursion of 4mm. The lost particles are relative to the number of halo particles entering the studied structure. One can see that most of the particles are lost in the quadrupole and the drift thereafter.

The right plot in Fig.1 shows the loss when a step in Y of 2mm in the drift between the dipole and quadrupole has

been introduced. This corresponds to the tolerances of the alignment errors of the beam screen. We see this causes strong losses at the point where the step is introduced.
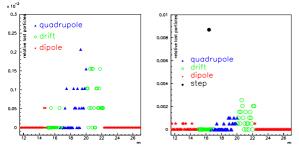

Figure 1: Longitudinal beam loss distribution along a part cell of the LHC for 450GeV. Left: Vertical orbit excursion of 4mm. Right: Beam screen misalignment error of 2mm in Y between the dipole and quadrupole.

Hence, particle losses happen along magnets with high beta-functions. In addition mechanical beam screen limitations can cause strong local losses.

3 DETECTOR SIGNALS AND POSITIONS

At the positions, where most of the beam losses are expected, simulations of the particle fluences outside the cryostat and induced by lost protons at the aperture have been performed with the Monte Carlo Code Geant 3.21.
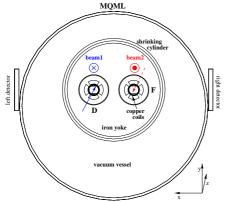

Figure 2: Cross-section of the MQML quadrupole in Q10. The magnet is (de)focusing for beam2 (beam1) in X.

3.1 Simulation procedure

The geometry used in this simulation corresponds to the dispersion suppressor. Calculations for the arc have already been presented in [2]. The arrangement consists of four quadrupole elements (Q8-Q11) separated by two dipoles (MBA, MBB), respectively. The layout is based on optics version 6.3 and includes also the various corrector magnets. In addition the magnetic field maps [5] for the quadrupoles and dipoles are comprehended. Fig.2 shows a cut of the simulated geometry of the quadrupole MQML in Q10. It is assumed that lost beam particles hit the beam screen under an angle of typically 0.25mrad (results of other angles vary only marginally) in the horizontal (vertical) plane when the magnet is focusing (defocusing) in X. The simulated shower particles

produced by lost protons are counted in the two detectors placed all along the cryostat on both sides (Fig.2). Also the energy deposition in these elements is calculated.

Fig.3 gives a typical example for both left and right detector signals of shower particles, which are induced by point like losses of beam1 and beam2 in the middle of the quadrupole MQML. For beam1 most of the induced signals are in the left detector. The shower maximum is about 1m after the beam loss location. The shower width is 0.5m. For one lost proton with 7TeV $1 \cdot 10^{-2}$ charged particles/p/cm^2 are observed. The second shower maximum is due to the gap between the quadrupole (MQML) and the dipole (MBA). In the right detector only a small signal from beam1 can be seen in the gap. These arguments are also all valid for beam2.
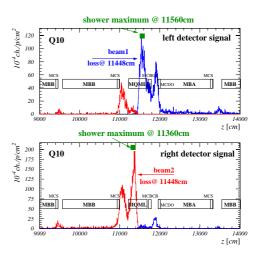

Figure 3: Simulated detector signals of shower particles, which are induced by point like losses of beam1 and beam2 in the middle of the quadrupole MQML. Top: Left detector signal along the cryostat. Bottom: Right detector signal along the cryostat.

3.2 Detector positions

Positioning beam loss monitors at the shower maxima locations fulfils the requirements for the distinction between the two beams and for localising the beam losses.

But this is just the ideal case of point losses. Beam losses can also be equally distributed in a magnet as shown in Chapter 2 (Fig.1). Then the peaks in Fig.4 are smeared along the quadrupole. However, simulations show that the beams can still be well distinguished. The signal rate would then be $4 \cdot 10^{-3}$ charged particles/p/cm^2 at the above-proposed position. In order to localize the losses, the signals of several detectors can be connected.

As also shown, we can expect high loss rates where the beam screens are mechanically connected. Since this happens always in the gaps between the magnets, the expected signals are very high. For 7TeV $6 \cdot 10^{-2}$ charged particles/p/cm^2 hit the detector at its appropriate position.

Hence, for each beam a set of three monitors around the quadrupole should be sufficient to detect beam losses.

4 BEAM LOSS DETECTOR

Ionisation chambers will be used as beam loss monitors. The baseline layout is a N_2 filled cylinder with a surface of $80cm^2$, a length of 19cm and a bias voltage of V=800-1000V. Fig.4 shows the minimal and maximal chamber current that corresponds to the quench levels for 450GeV and 7TeV. These curves comprise the simulated numbers of charged particles per lost beam protons for different detector locations and loss scenarios. The averaged energy deposition of the charged particles in the detector is nearly a factor 2 higher than for minimum ionising particles, since most of the charged particles passing through the detector have an energy of less than $\beta\gamma=4$.
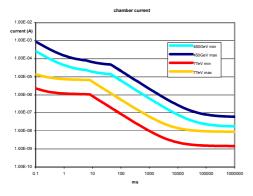

Figure 4: The chamber current that corresponds to quench levels for 450GeV and 7TeV for different detector positions and different loss distributions as a function of the loss duration.

4.1 Read-out electronics

The particle losses are measured with an analog front end and transmitted to the surface, where the final evaluation takes place. To measure the chamber signal, a current-to-frequency converter (CFC) was designed. It works on the principle of balanced charge and is shown below.
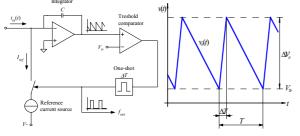

Figure 5: Principle of the charged balanced current-to-frequency converter (CFC).

The signal current is integrated during the whole period T. If a constant chamber current is assumed, the integrator output ramps down. After reaching a threshold, the reference current I_{ref} is induced into the summing node of the op amp for a fixed time ΔT, driving the integrator output back again (see Fig.5). The output frequency is related to the chamber current by

$$f = \frac{\bar{i}_{in}}{I_{ref}\Delta T}.$$

The performance of the CFC was tested using a Keithley current source. The diagram in Fig.6 depicts the output frequency versus input current and the linearity error. The circuit shows an error of less than 5% between 20pA and 1mA. The error was derived by linearizing the characteristic through 1µA/5kHz.
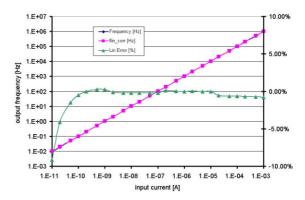

Figure 6: Output frequency of the CFC versus input current with linearity errors.

The output frequency is evaluated by local 8-bit counters, which count the reset pulses. Every 40µs (twice a turn) the counter values are loaded into parallel-to-serial shift registers. Six beam loss channels are cascaded to form a serial data stream.

5 SUMMARY

Longitudinal beam loss distribution studies show that losses concentrate on locations with high β-functions or where mechanical limitations of the aperture can be assumed. From shower simulations at the different loss locations we see that a set of six detectors around the quadrupoles is sufficient for localising the beam losses and to distinct between the two beams. The expected ionisation chamber current, equivalent to the quench levels, varies between 500pA and 1mA depending on the different loss distributions and detector positions. This dynamic range of $~10^8$ in the chamber signal can be measured with a charged balanced current-to-frequency converter (CFC).

6 ACKNOWLEDGMENT

We thank Ralph Assmann for generating the phase space distribution of the tertiary halo.

7 REFERENCES

[1] J.B. Jeanneret et al., LHC Project Report 44, CERN, (1996).
[2] A. Arauzo-Garcia et al., CERN-SL-2001-027-BI, CERN, (2001).
[3] R. Assmann et al., These proceedings, (2002).
[4] V. Kain et al., These proceedings, (2002).
[5] S. Russenschuck, CERN-99-001, (1998).